RSC Advances

ROYAL SOCIETY OF CHEMISTRY

www.rsc.org/advances

Journal Name

Dynamic Article Links ▶

ARTICLE TYPE

Highly-ordered Maghemite/Reduced Graphene Oxide Nanocomposites for High-performance Photoelectrochemical Water Splitting

Sundaram Chandrasekaran[a], Seung Hyun Hur[a*], Eui Jung Kim[a], Balasubramaniyan Rajagopalan[a], Kadumudi Firoz Babu[a], Velusamy Senthilkumar[b], Jin Suk Chung[a], Won Mook Choi[a] and Yong Soo Kim[b]

5

Highly ordered γ-Fe_2O_3/reduced graphene oxide (RGO) was synthesized via a facile solution technique combined with calcination at various temperatures. The maghemite iron oxide structure was obtained on 10 the GO surface and improved crystallinity of γ-Fe_2O_3 was observed as the calcination temperature increased. The prepared highly ordered maghemite structure on RGO exhibited an excellent water splitting performance under UV light (~360 nm) illumination. The photocurrent density of RGO/γ-Fe_2O_3 calcined at 500°C was 6.74 mA/cm^2 vs. RHE with high incident photon to current conversion efficiency (IPCE) of 4.7%, was achieved. This photocurrent density and the IPCE values are 3.7 times and 4 times 15 higher than that of pristine iron oxide, respectively.

1. Introduction

Production of hydrogen and oxygen from photocatalytic water splitting has attracted substantial attention as a potential means of renewable energy production with no reliance on fossil fuels and 20 no carbon dioxide emission[1, 2]. The hydrogen production from water by the solar energy is essential to constructing clean energy systems in order to solve the energy and environmental issues together. Even though various photocatalysts have been explored, efficient materials for water splitting into H_2 and O_2 have not 25 been found yet[3, 4]. In this regard, an important part of the scientific community is currently focusing on the synthesis of novel nanostructured materials that are capable of absorbing the photonic energy emitted by the sun or external source with a high efficiency of its conversion into chemical or electrical energy. 30 The photocatalytic water splitting is still a challenging reaction even if the research history is long. Usually, photolysis or photo splitting of water into gaseous O_2 and H_2 is described by equation[5],

$$35 \quad H_2O \xrightarrow{h\nu} H_2 + \tfrac{1}{2}O_2 \qquad (1)$$
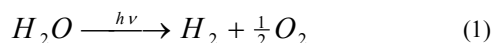
The rate of water splitting by photoelectrochemical cell (PEC) can be increased significantly when artificial UV light sources are used [5].

40 Recently, various metal oxides (such as TiO_2, ZnO, WO_3, and CoO) and graphene based metal oxide composites have been investigated for PEC water splitting[6-12]. Among them, Iron oxides (Fe_3O_4, α-Fe_2O_3 and γ-Fe_2O_3 etc.) have received much attention due to their favourable optical band gap, excellent chemical 45 stability, natural abundance, and low material cost[13-16]. The maximum theoretical efficiency of solar-to-hydrogen (STH) conversion is 16.8 % so far, however, the reported value of STH

for iron oxide is much lower than the expected value due to its very short lifetime of photo generated charge carriers (<10 ps) 50 and short hole diffusion length ($\sim$ 2-4 nm) [17].

Lately, graphene and graphene based hybrid materials have drawn great attention due to their unique microstructures and properties, which promote their extensive potential application in many fields[18, 19]. Moreover, the properties of graphene oxide 55 (GO) and mildly reduced graphene oxide (RGO) prepared by the chemical method can be easily tailored compared with the graphene grown by the chemical vapour deposition (CVD) due to the formation of various functional groups such as the hydroxyl, carbonyl, and carboxyl groups on the graphene surface, which 60 enables GO and RGO more easily modified by other materials[20-24]. Therefore, semiconductor nanoparticles assembled on the surface of GO are believed to provide a new way to design high-performance energy harvesting electrode materials. Even though iron oxide/graphene composites have been extensively studied for 65 use as an anode material for Li-ion batteries[25], super capacitors[26, 27], sensors[28] and catalysts[29, 30], to the best of our knowledge, no PEC study of RGO/γ-Fe_2O_3 has been reported in the literature so far. There are few reports available on the electrochemical behaviour of RGO-maghemite (γ-Fe_2O_3) nanocomposites [25, 31, 32], 70 while many literatures are available for magnetite and hematite based composites[13-16]. Moreover, due to a lack of studies on maghemite/graphene composites, the actual nature of iron oxide is still unrevealed and most of the previous reports on iron oxide/graphene composites have assumed that iron oxide has 75 magnetite phase.

Although nano-sized iron oxide and iron oxide composites made by atmospheric pressure chemical vapor deposition (APCVD) [15, 33] and atomic layer deposition (ALD) [34] have shown excellent PEC performance, these techniques require special

instruments such as atomizers or CVD or ALD. Moreover, ALD systems need toxic and flammable metal-organic precursors. In this paper, we report highly efficient photocatalytic materials that exhibit high energy conversion efficiency and excellent
5 operational stability. We fabricated crumpled RGO/iron oxide (maghemite) nanocomposites by a facile solution technique. In addition, the structure of iron oxide anchored on GO was accurately identified in this work. After calcination at 300, 400 and 500 °C for 4 h (for sample identification the as-prepared,
10 300, 400 and 500 °C calcined samples are denoted as RGO-M1, RGO-M2, RGO-M3 and RGO-M4, respectively), the PEC performances were highly improved. The overall water splitting photocurrent density of 6.74 mA/cm^2 with high incident photon to current conversion efficiency (IPCE) of 4.7% was achieved for
15 the RGO-M4 (under UV light ~ 360 nm), which is the highest IPCE for RGO based Iron oxide photocatalysts under UV light.

2. Materials and Methods

2.1. Synthesis of GO and RGO/γ-Fe₂O₃ nanocomposites

Graphene oxide (GO) was synthesized from graphite powder
20 using a modified Hummers' method. Briefly, 1 g of graphite and 0.5 g of sodium nitrate were mixed, which was followed by the addition of 23 ml of concentrated sulfuric acid under constant stirring with a magnetic stirrer. After 1 h, 3 g of KMnO$_4$ was gradually added to the above solution while keeping the
25 temperature below 20°C to prevent overheating and explosion. The mixture was stirred at 35 °C for 8 h and the resulting solution was diluted with 500 ml of deionized water under vigorous stirring. To ensure the completion of the reaction with KMnO$_4$, the diluted mixture was further treated with 30% H$_2$O$_2$ solution (5
30 ml). The resulting suspension was washed with HCl and H$_2$O, respectively, which was followed by filtration and drying to produce GO.

To synthesize RGO/γ-Fe₂O₃ nanocomposites, 20 mg of GO was first dispersed in deionized water (40 ml) with vigorous
35 stirring at 70°C to obtain a homogeneous dispersion. Then, the GO solution was added to 0.5 mol/L of Iron (III) chloride aqueous solution (80ml) and the mixture was stirred for 1 h. An ammonia/ethanol solution with a 1:1 (v/v) ratio (4ml) was added to the above solution. Finally, RGO/γ-Fe₂O₃ precipitates were
40 collected, washed with distilled water, and dried at 70°C for 15 h. Then, the dried sample was further calcined at 300°C, 400°C and 500°C for 4 h. Pure iron oxide was prepared by the same procedure without RGO.

2.2. Instrumental analysis

45 X-ray diffraction (XRD; Rigaku) spectroscopy with Cu-Kα radiation was used to identify the crystalline phases. Field emission scanning electron microscopy (FE-SEM; JSM 6500F) was used to investigate the surface morphology of RGO/γ-Fe₂O₃ nanocomposites. Transmission electron microscopy (TEM; JEOL
50 JEM 2100F) was used to analyse the micrograph images of the prepared samples. The functional groups were identified by using a Thermo Scientific Nicolet 380 FTIR spectrometer. Optical absorption measurements were taken on an Analytik Jena SPECORD210 Plus UV-Vis spectrometer. The vibrational,
55 rotational, and other low-frequency mode in the sample was analyzed using a Thermo Scientific DXR Raman

spectrophotometer. Materials composition and oxidation states of carbon and iron atoms in the RGO/γ-Fe₂O₃ nanocomposites were analyzed using a Thermo Scientific K-alpha X-ray photoelectron
60 spectrometer (XPS).

2.3 Photoelectrochemical analysis

The photoelectrochemical tests were carried out using cyclic voltammetry (CV) with a three cell system by an electrochemical working station (Gamry instrument). The working electrodes
65 were prepared with the RGO/γ-Fe₂O₃, carbon black and polyvinylidene fluoride (PVDF) binder in a weight ratio of 8:1:1. The slurry was then coated on one side of thin Cu foil with a size of 1 x 1 cm^2 and dried for 2 h at 60°C in an oven. The mass of the electrode material was about 4 mg. The reference electrode and
70 counter electrode were Ag/AgCl and Pt, respectively. The other side of the Cu foil was masked with a non-conducting tap. The measured potential vs. Ag/AgCl was converted to the reversible hydrogen electrode (RHE) scale using the Nernst equation,

$$E_{RHE} = E_{Ag/AgCl} + 0.241V + 0.0591 \times pH \text{ at } 25°C$$

75 The PEC water splitting performance of the photoanodes was evaluated using 1.0 M NaOH buffer solution (pH = 13.6) in a three electrode chemical cell under 360 nm UV light illumination.

3. Results and Discussion

The XRD patterns of graphite, RGO, pristine iron
80 oxide, as-prepared and calcined RGO/ γ-Fe₂O₃ are shown in Fig. 1. The XRD pattern of the pristine iron oxide agreed well with the JCPDS file (No. 89-0951), indicating that the pristine iron oxide nanopowder has magnetite structure. On the contrary, RGO-M1 (as-prepared RGO/γ-Fe₂O₃) and RGO-M2 to RGO-M4
85 (calcined RGO/γ-Fe₂O₃) exhibited major (111), (220), (311) and (400) peaks, meaning that RGO induced the structural change of iron oxide. No structural changes but the intensity increase of iron oxide in the RGO/γ-Fe₂O₃ was observed during calcination, which indicates the calcination process was responsible for the
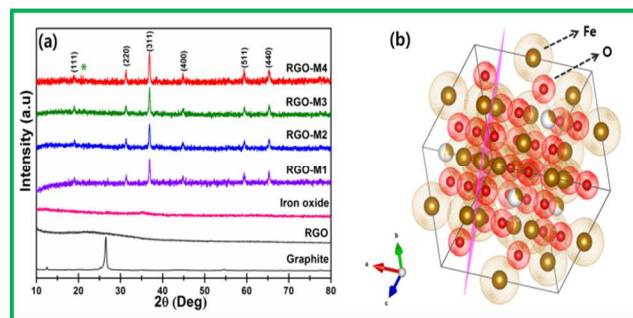90 preferred orientations[31, 32].

Fig 1. (a) The XRD patterns of graphite, reduced graphene oxide, iron oxide and RGO/ γ-Fe₂O₃ samples (* indicates RGO peak). (b) Atomic arrangement of γ-Fe₂O₃ in a unit cell and representation of (311) plane.

95 The presence of iron nanoparticles reduces the aggregation of graphene sheets, which results in less stacking of GO sheets. As a result, a weak GO related peak was observed in the XRD patterns. Maghemite (γ-Fe₂O₃) and magnetite (Fe₃O₄), two main forms of iron oxide, have cubic inverse spinel structure and they are very
100 similar in structure to each other. The distinct feature of maghemite is the presence of iron vacancies in the sub lattice. The cation or vacancy distribution in octahedral positions can

give rise to several crystal symmetries in maghemite with the corresponding differences in the XRD patterns (Fig. 1b). Usually, disordered maghemite particles belong to the space group Fd3m[25]. The spinel structure of γ-Fe_2O_3 contains cation vacancies that can
5 be ordered (tetragonal superstructure), partially ordered (cubic superstructure), or completely disordered with a high probability of the aggregated vacancies[35]. The precise nature of the ordering in γ-Fe_2O_3 particles with GO is still unclear[35, 36]. The observed and standard *d*-values for the iron oxide in the RGO/γ-Fe_2O_3
10 nanocomposites fabricated in this study agree well with JCPDS card no. 39-1346, confirming the cubic symmetry of maghemite (γ-Fe_2O_3), i.e. Fe^{3+} in octahedral sites and O in close-packed cubic arrangement (The maghemite structure was further confirmed by SAED patterns, which will be discussed in TEM
15 analysis). It is well known that during the heat treatment of GO/γ-Fe_2O_3 iron atoms can interact with the oxygen related functional groups of GO and form Fe-O-C bonds, which results in the formation of maghemite structure of iron oxide on the GO sheets. Further, the functional groups on the surface of GO disappear
20 when GO is thermally reduced and more π electrons on C atoms are regenerated by the restoration of sp^2 networks. Thus, the unpaired π electrons are attracted to free Fe atoms, which results in the preferred growth of γ-Fe_2O_3 on the surface of RGO. From the Debye-Scherer formulae[31], the broad diffraction peaks are
25 indicative of small-sized iron oxide nanoparticles (20-24 nm) in

the RGO/γ-Fe_2O_3 nanocomposites. The functional groups of the crumpled RGO/γ-Fe_2O_3 were identified from FTIR spectra in Fig. 2a. Absorption peaks at 586.94, 632.06, and 793.60 cm^{-1} can be ascribed to the maghemite structure of iron oxide[37]. The peak
30 around ~586 cm^{-1} is attributed to Fe-O bonds, and the enhanced intensity of Fe-O peak is due to iron oxide loaded to RGO[38]. Serna *et al*.[39] reported that a less-ordered maghemite (γ-Fe_2O_3) structure is evidenced by multiple lattice absorption bands within 800 cm^{-1}. The broad peaks at around 800 and 580 cm^{-1} is the
35 characteristic of well-ordered γ-Fe_2O_3[35]. No peaks appeared at 3438 and 3150 cm^{-1}, which strongly implies that α-FeOOH is absent in the prepared iron oxides. The peaks at 1638.39 cm^{-1} and 2357 cm^{-1} were due to the OH bending of water and the presence of atmospheric CO_2, respectively. The stretching vibrations of
40 epoxy C-O (1226.92 cm^{-1}), weak aromatic C=C (1578 cm^{-1}), and carboxyl O-C=O (1386.11 cm^{-1}) bonds were observed in RGO/iron oxide samples, which can be ascribed to the functional groups of GO and RGO[40]. As the calcination temperature increased, some functional groups present in the RGO-M1
45 disappeared due to the thermal reduction of functional groups in GO.

Fig. 2b represents the Raman spectra of RGO/γ-Fe_2O_3 nanocomposites. The spectral values are in good agreement with the standard Raman spectrum of maghemite[41, 42].
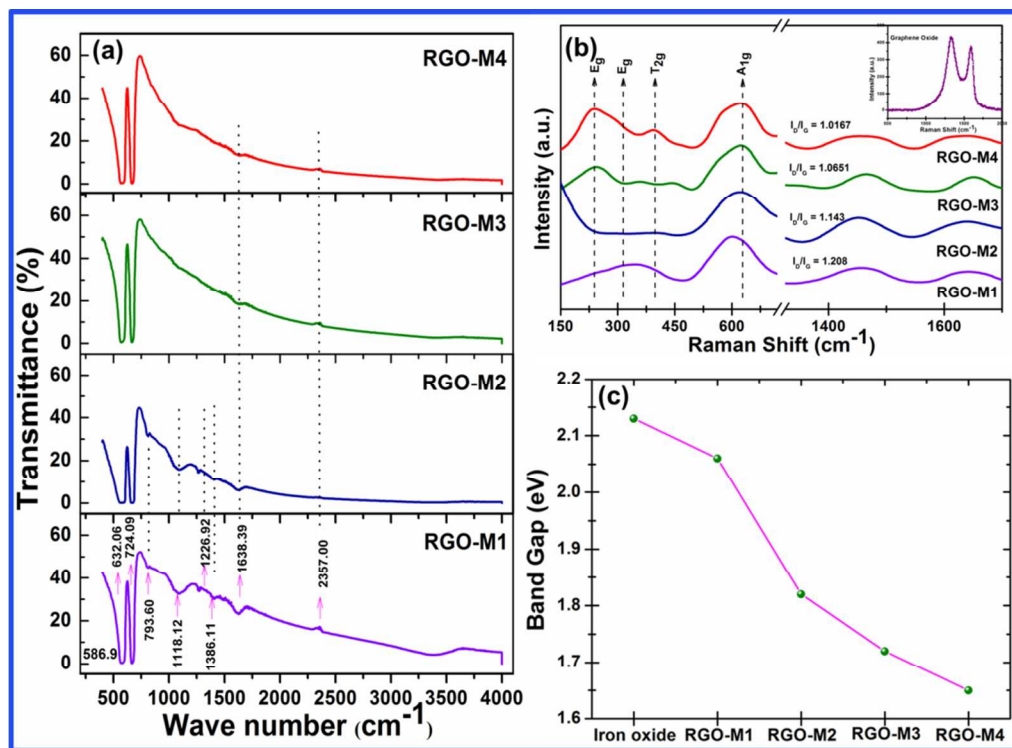

Fig 2. (a) The FTIR spectra of RGO/γ-Fe_2O_3 nanocomposites. (b) The Raman spectra of RGO/γ-Fe_2O_3 nanocomposites (the inset represents the Raman spectra of graphene oxide). (c) Band gap values of iron oxide and RGO/γ-Fe_2O_3 samples.

For maghemite structure[43], the net structure is spinel symmetry
55 with randomly distributed vacancies in its structure. The projected vibrational modes of the first Brillouin zone center of a spinel structure is given as

$$\Gamma_{vib} = A_{1g} + E_{1g} + T_{1g} + 3T_{2g} + 2A_{2u} + 2E_u + 4T_{1u} + 2T_{2u}$$

In the above equation, excluding T_{1g}, A_{2u}, E_u, T_{1u} and T_{2u} modes
60 (Raman inactive modes), all modes of vibrations are easily observable for maghemite spinel structure in the Raman spectra.

The enduring symmetrical modes like A_{1g}, E_g, and T_{2g} are Raman active modes. As shown in Fig. 2b, three active modes were observed for maghemite phase, i.e. ~ 263 cm^{-1} (E_g : Fe–O symmetric bending), ~ 345 cm^{-1} (E_g : Fe–O symmetric stretching),

5 ~ 395 cm^{-1} (T_{2g} : Fe–O asymmetric bending) and ~ 665 cm^{-1} (A_{1g} : symmetric stretching). The active modes of the Raman signal varies with materials preparation conditions and the vacancies in the maghemite crystal unit cell[37]. The weak Raman signal is the result of poor scattering properties of maghemite[42]. Compared

10 with other samples, the RGO-M4 samples exhibited a red-shifted peak frequency for the main A_{1g} peak, indicating a greater degree of maghemite crystallinity. The RGO in the RGO/γ-Fe$_2$O$_3$ nanocomposites are more amorphous than GO and the broadened and shifted band is due to the destruction of conjugated system in

15 graphite. Compared with other samples, a smaller I_D/I_G ratio for the RGO-M4 (1.02) implies a larger sp^2 domain size at higher calcination temperature[31]. The optical band gap of pristine iron oxide (~ 2.13 eV) and RGO/γ-Fe$_2$O$_3$ nanocomposites was evaluated from the UV-Vis absorption spectra using Tauc relation

20 $((\alpha h\upsilon)^{1/2}$ vs. the photon energy where α is the absorption coefficient) as shown in Fig. 2c and Fig. S1. Similar to previous results acquired for RGO-metal oxide nanocomposites, the RGO/γ-Fe$_2$O$_3$ composites exhibited a narrower band gap after the modification of γ-Fe$_2$O$_3$ with RGO and subsequent calcination.

25 This phenomenon can be attributed to the formation of metal-O-C chemical bonds in the RGO/γ-Fe$_2$O$_3$ composites [44, 45].

Fig 4. TEM images and SAED patterns of (a-b) RGO-M1, (c-d) RGO-M2, (e-f) RGO-M3 and (g-h) RGO-M4 samples.

45 reflection). It should be noted that the increased crystallinity of γ-Fe$_2$O$_3$ compared with pure iron oxide denotes that GO affects the formation of maghemite crystalline structure.

The electronic state and the chemical composition of the samples were investigated by XPS. The XPS survey spectra

50 in Fig. S2 reveal the presence of Fe, C and O in the RGO/ γ-Fe$_2$O$_3$. As shown in Fig. 5, several XPS peaks appeared for iron oxide. In the observed XPS spectra, the major peaks at ~ 711.7 eV and ~ 725.1 eV associated with Fe$_{2p3/2}$ and Fe$_{2p1/2}$ core-level binding energies of γ-Fe$_2$O$_3$ on RGO[25]. The nature of the γ-Fe$_2$O$_3$

55 was clearly revealed by simulating the observed spectra. It shows that, ~ 710.7eV, 713.2eV and 718.7 eV (satellite peak) is ascribed to Fe$_{2p3/2}$ state. The presence of satellite peak at ~ 718.7 eV is characteristic for maghemite [47]. The peaks at 725.1 eV and 732.7 eV well documented to Fe$_{2p1/2}$ state of iron oxide[26]. The Fe^0 (709

60 eV) peak was not observed and only Fe^{2+} and Fe^{3+} states were detected in the XPS spectra as the γ-Fe$_2$O$_3$ nanoparticles were oxidized. The O1s core level XPS spectra of as prepared sample showed two peaks at 529.96 and 531.84 eV, corresponding to Fe-O and Fe-O-C bond formations, respectively. Further calcination,
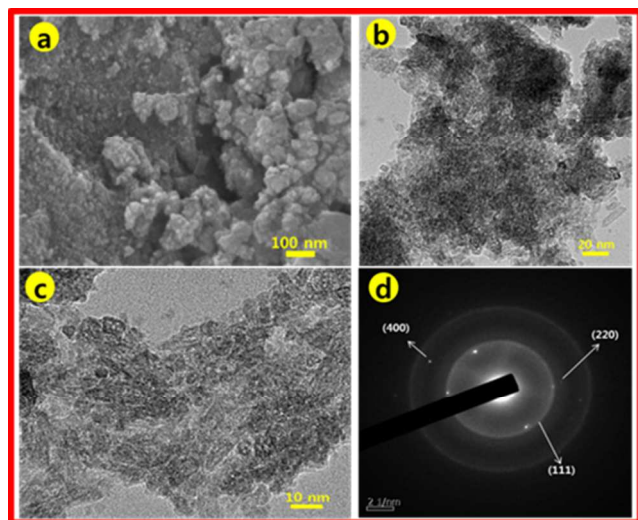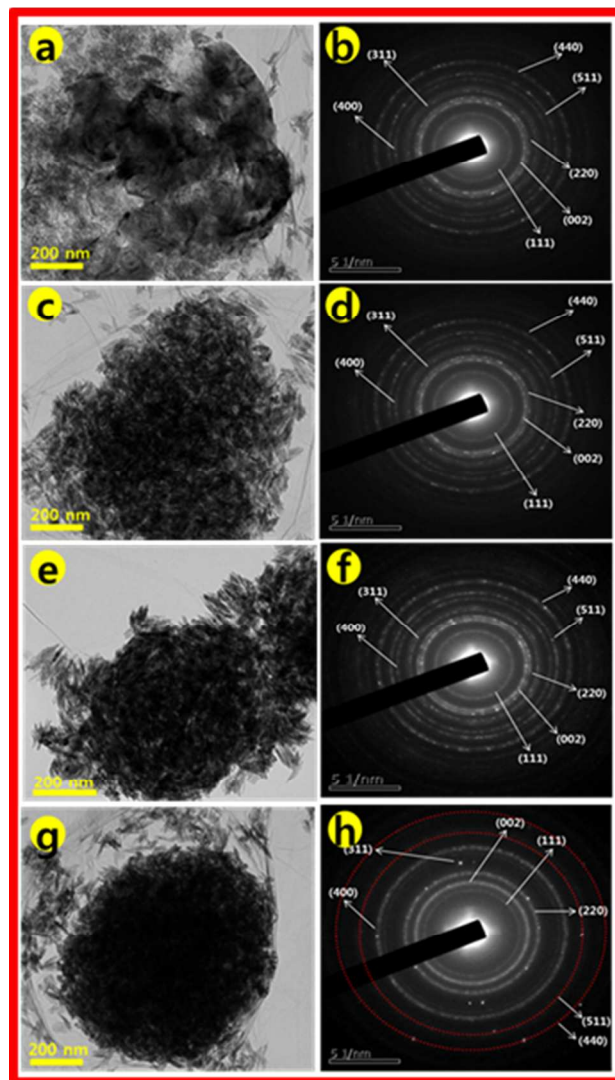
Fig 3. (a) FE-SEM, (b-c) TEM images at various scales and (d) SAED
30 pattern of pristine iron oxide.

Fig. 3(a, b and c) represents the FE-SEM and TEM images of the pure iron oxide sample. It clearly shows that the sample consists of agglomerated spherical particles of diameter ranging from 15 to 25 nm. Fig. 3d displays the electron diffraction

35 (SAED) pattern indexed with the cubic symmetry of the magnetite phase, which is in good agreement with JCPDS file (No.89-0951) and the above XRD results. Fig. 4 illustrates the TEM images and SAED patterns of RGO/ γ-Fe$_2$O$_3$ nanocomposites. As shown in Fig. 4, large amounts of iron oxide

40 nanoparticles are uniformly decorated on RGO[46] and the intensity of SAED pattern evidently displays the graphene (002 plane -

the binding energy values were found to be shifted slightly in positive are due to the formation of coordinated oxygen in the composites (Fig S3 and Table S1)[48, 49]. The XPS data strongly support the XRD, FTIR and Raman results and confirm the high order of γ-Fe$_2$O$_3$ on the surface of GO in all prepared nanocomposites.
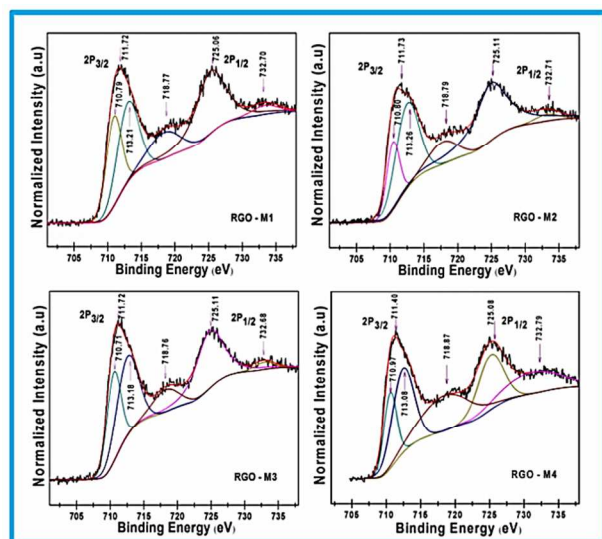

Fig 5. XPS spectra (Fe$_{2p}$ state) of RGO/γ-Fe$_2$O$_3$ samples.

The linear sweep voltagrams of pure iron oxide, as-prepared and calcined samples are shown in Fig. 6a. In the absence of UV light illumination, no oxidation photocurrent was obtained, indicating that all the electrodes are inactive toward OER in the dark condition. When the UV light was illuminated, all the electrodes exhibited a considerable oxidation photocurrent. The maximum photocurrent density was 1.83, 3.04, 3.39, 4.65 and 6.74 mA/cm^2 for pristine iron oxide, RGO-M1, RGO-M2, RGO-M3 and RGO-M4, respectively. This result indicates that photocatalytic performance of iron oxide can be significantly improved by its hybridization with GO and calcination process. As described in Fig. 6b, the RGO serves as an electron sink to facilitate the exciton separation and store the separated electron[47]. The saturated photocurrent density of the RGO-M4 was ca. 6.74 mA/cm^2, which is 3.7 times higher than that of the pristine iron oxide and 2.3 times higher than that of the RGO-M1. An increase in photocurrent with calcination temperature is believed to be the result of reduced defect density (i.e. highly ordered γ-Fe$_2$O$_3$) in RGO/γ-Fe$_2$O$_3$ samples.

The photoconversion efficiency of the sample was calculated using the following equation:

$$\eta = I(1.23 - V)/J_{light} \qquad (2)$$

where V is the applied bias vs. RHE, I is the photocurrent density at the measured bias, and J$_{light}$ is the irradiance intensity of 500 mW/cm^2. As shown in Fig. 7a, the optimal conversion efficiency of the pure iron oxide was 0.21% vs. RHE. On the other hand, RGO-M1, RGO-M2, RGO-M3, and RGO-M4 showed higher efficiency of 0.31%, 0.39%, 0.53% and 0.76 %, respectively, at a similar applied bias. This indicates that the hybridization of γ-Fe$_2$O$_3$ with graphene and thermal treatment substantially enhance the photoconversion efficiency of γ-Fe$_2$O$_3$.

To obtain a relationship between photo activity and light absorption of RGO/γ-Fe$_2$O$_3$, we have quantitatively investigated the photo activity of RGO/γ-Fe$_2$O$_3$ as a function of wavelength of incident light. In comparison to the photocurrent density, the photocurrent density, the photocurrent as a function of the wavelength and incident photon to current conversion efficiency (IPCE) is a more appropriate parameter to characterize the photoconversion efficiency of different photo anodes as it is independent of the light sources. IPCE can be calculated by the following equation:

$$IPCE (\lambda) = 1240 J(\lambda)/ \lambda E_\lambda(\lambda) \qquad (3)$$

where J(λ) is the measured photocurrent density (mA/cm^2) and E$_\lambda$(λ) is the incident light power density (mW/cm^2) for each wavelength (λ in nm). As shown in Fig. 7b, RGO/γ-Fe$_2$O$_3$ exhibited significantly enhanced photo activity in the UV region compared with pure iron oxide. Importantly, the IPCE of the RGO-M4 was 4.7% at 360 nm, which is ~ 4 times higher than that of the pure iron oxide and ~2.5 times higher than that of RGO-M1. The IPCE values obtained by this study was compared with already reported values presented in Table 1.The highly extended light absorption band of iron - oxide after GO decoration in the RGO/γ-Fe$_2$O$_3$ makes more photo-induced holes contribute to the oxidation current under illumination[13]. In addition, small-sized γ-Fe$_2$O$_3$ nanoparticles may further improve the PEC efficiency of OER by decreasing the hole diffusion distance and increasing the RGO/γ-Fe$_2$O$_3$-solution interfacial area. Applying a positive potential to the photoanode facilitates the hole injection process and accelerates the hole diffusion to the photoanode/solution interface where the holes oxidize water[50-58].
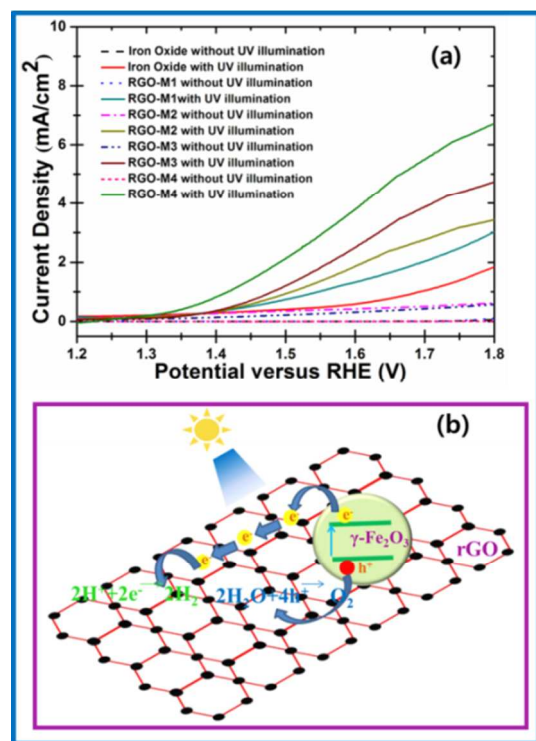

Fig 6. (a) Linear sweep voltamograms of pristine iron oxide and RGO/γ-Fe$_2$O$_3$ samples at a scan rate of 20 mV/sec in 1.0 M NaOH electrolyte. (b) Schematic diagram of water splitting by RGO/γ-Fe$_2$O$_3$

Table1. The Incident Photon to Current Conversion efficiency of iron oxide-based photocatalysts (1.0 M NaOH electrolyte was used).

Photocatalyst	Method	IPCE (%) value at 360 nm	Ref
$\alpha\text{-Fe}_2\text{O}_3$	AACVD	0.2	[15]
$\alpha\text{-Fe}_2\text{O}_3$	Deposition annealing	3.2	[50]
$\text{Pt-}\alpha\text{-Fe}_2\text{O}_3$	Electro deposition	4.0	[52]
$\text{n-Fe}_2\text{O}_3$	Spray pyrolysis	1.8	[53]
$\alpha\text{-Fe}_2\text{O}_3\text{/graphene}$	Spray pyrolysis	3.5	[57]
$\alpha\text{-Fe}_2\text{O}_3\text{/CNT}$	Spray pyrolysis	4.2	[57]
Fe_3O_4	Solution method	1.2	Present work
RGO-M4 (RGO/$\gamma\text{-Fe}_2\text{O}_3$ (500°C calcined))	Solution method	4.7	Present work
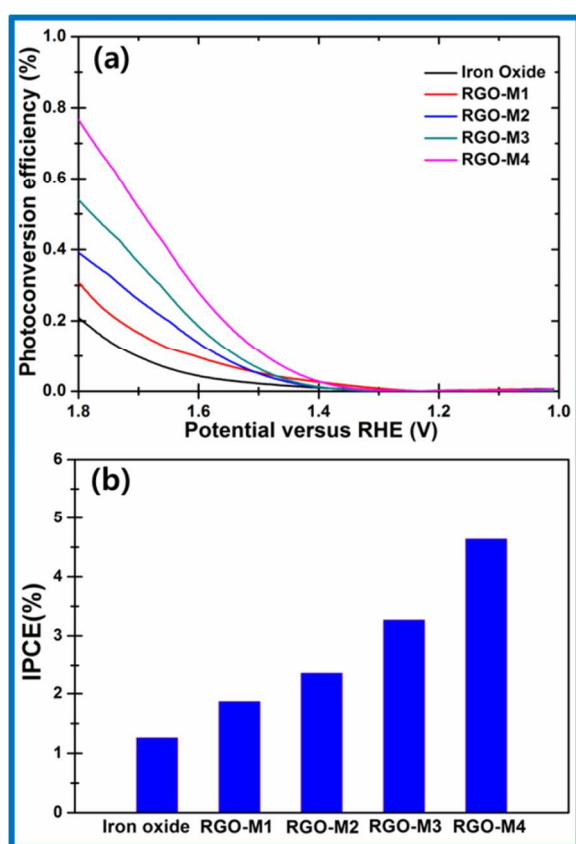
Fig 7. (a) Chemical energy conversion efficiency of pristine iron oxide and RGO/$\gamma\text{-Fe}_2\text{O}_3$ samples (scan rate of 20 mV/s in 1.0 M NaOH). (b) Incident photon to current conversion efficiency of iron oxide and RGO/$\gamma\text{-Fe}_2\text{O}_3$ nanocomposites.

The photo-induced electrons are spontaneously -injected from the conduction band of iron oxide into that of graphene. Further, the applied positive potential that provides a driving force for the electrons to transfer to the RGO could increase the charge separation and suppress the charge recombination, which leaves long-lived holes in the $\gamma\text{-Fe}_2\text{O}_3$ to oxidize water increasing the photocatalytic water splitting rate.

4. Conclusions

In this work, highly ordered maghemite/RGO nanocomposites were synthesized via a facile and cost effective solution technique. The maghemite iron oxide structure was formed on the GO surface due to the formation of Fe-O-C bonds between Fe and GO, which was confirmed by the TEM, Raman, XPS, XRD and FTIR analyses. The photocatalytic activity of RGO/$\gamma\text{-Fe}_2\text{O}_3$ nanocomposites was higher than that of pure iron oxide due to the enhanced light absorption and accelerated charge separation when iron oxide was anchored on GO. As the calcination temperature increased, the photocatalytic activity of RGO/$\gamma\text{-Fe}_2\text{O}_3$ nanocomposites was increased due to the improved iron oxide crystallinity and decreased defect density. The out-standing water splitting performance of the RGO/$\gamma\text{-Fe}_2\text{O}_3$ composites opens promising prospects for a new generation of photocatalyst exploiting the synergistic effects of the PEC cell.

Acknowledgements

Notes and references

[a] *School of Chemical Engineering, University of Ulsan, Daehak-ro, 102, Nam-gu, Ulsan 680-749, South Korea.* Fax: +82 52 259 1689; Tel:+82 52 259 1028; E-mail: shhur@ulsan.ac.kr
[b] *Department of Physics and Energy Harvest-Storage Research Center, University of Ulsan, Ulsan 680-749, South Korea.*

†Electronic Supplementary Information (ESI) available: [details of any supplementary information available should be included here]. See DOI: 10.1039/b000000x/

‡ Footnotes should appear here. These might include comments relevant to but not central to the matter under discussion, limited experimental and spectral data, and crystallographic data.

1. M. Gratzel, *Nature*, 2001, 414, 338-344.
2. J. Li and N. Wu, *Catal. Sci.Tech.*, 2015. 4440-4441
3. M. G. Walter, E. L. Warren, J. R. McKone, S. W. Boettcher, Q. Mi, E. A. Santori and N. S. Lewis, *Chem.Rev.,* 2010, 110, 6446-6473.

4. W. Rüttinger and G. C. Dismukes, *Chem. Rev.*, 1997, 97, 1-24.

5. L. Wang, C.-Y. Lee and P. Schmuki, *Electrochem.Commun.*, 2013, 30, 21-25.

6. T. Hisatomi, J. Kubota and K. Domen, *Chem.Soc.Rev.*, 2014, 43, 7520-7535.

7. Y. Lin, G. Yuan, R. Liu, S. Zhou, S. W. Sheehan and D. Wang, *Chem.Phys.Lett.*, 2011, 507, 209-215.

8. T.-F. Yeh, J. Cihlář, C.-Y. Chang, C. Cheng and H. Teng, *Mater. Today.*, 2013, 16, 78-84.

9. P. V. Kamat and J. Bisquert, *J. Phys. Chem C.*, 2013, 117, 14873-14875.

10. S. Chandrasekaran, *Sol. Energ. Mat. Sol. Cells.*, 2013, 109, 220-226.

11. S. Chandrasekaran, W. M. Choi, J. S. Chung, S. H. Hur and E. J. Kim, *Mater. Lett.*, 2014, 136, 118-121.

12. S. Chandrasekaran, *J.Nanoeng.Nanomanuf.*, 2011, 1, 242-247.

13. T. Jin, P. Diao, Q. Wu, D. Xu, D. Hu, Y. Xie and M. Zhang, *Appl. Catal. B.*, 2014, 148–149, 304-310.

14. H. Gao, C. Liu, H. E. Jeong and P. Yang, *ACS Nano*, 2011, 6, 234-240.

15. A. A. Tahir, K. G. U. Wijayantha, S. Saremi-Yarahmadi, M. Mazhar and V. McKee, *Chem. Mater.*, 2009, 21, 3763-3772.

16. I. Cesar, A. Kay, J. A. Gonzalez Martinez and M. Grätzel, *J. Am. Chem. Soc.*, 2006, 128, 4582-4583.

17. H. Dotan, O. Kfir, E. Sharlin, O. Blank, M. Gross, I. Dumchin, G. Ankonina and A. Rothschild, *Nat. Mater.*, 2013, 12, 158-164.

18. N. A. Zubir, C. Yacou, J. Motuzas, X. Zhang and J. C. Diniz da Costa, *Sci. Rep.*, 2014, 4,1-8.

19. Y. V. Pleskov, *Russ. J. Electrochem.*, 2003, 39, 328-330.

20. C. K. Chua and M. Pumera, *Chem.Soc. Rev.*, 2014, 43, 291-312.

21. H. P. Mungse and O. P. Khatri, *J. Phys.Chem C.*, 2014, 118, 14394-14402.

22. K. P. Loh, Q. Bao, G. Eda and M. Chhowalla, *Nat. Chem.*, 2010, 2, 1015-1024.

23. Y. Zhang, Z. Schnepp, J. Cao, S. Ouyang, Y. Li, J. Ye and S. Liu, *Sci. Rep.*, 2013, 3,1-8.

24. J. Wang, C. Zhang, Y. Shen, Z. Zhou, J. Yu, Y. Li, W. Wei, S. Liu and Y. Zhang, *J.Mater.Chem A.*, 2015, 3, 5126-5131.

25. S.H. Yu, D. E. Conte, S. Baek, D.-C. Lee, S.-K. Park, K. J. Lee, Y. Piao, Y.-E. Sung and N. Pinna, *Adv.Funct.Mater.,* 2013, 23, 4293-4305.

26. Q. Qu, S. Yang and X. Feng, *Adv.Mater.*, 2011, 23, 5574-5580.

27. P.C. Gao, P. A. Russo, D. E. Conte, S. Baek, F. Moser, N. Pinna, T. Brousse and F. Favier, *ChemElectroChem*, 2014, 1, 747-754.

28. T. Peik-See, A. Pandikumar, H. Nay-Ming, L. Hong-Ngee and Y. Sulaiman, *Sensors*, 2014, 14, 15227-15243.

29. A. Dey, P. Varma, J. Athar, H. Prasant, A. Sikder and S. Chattopadhyay, *R.Soc.Chem. Adv.*, 2014.5, 1950-1960.

30. J. Tuček, K. C. Kemp, K. S. Kim and R. Zbořil, *ACS Nano*, 2014, 8, 7571-7612.

31. I. T. Kim, A. Magasinski, K. Jacob, G. Yushin and R. Tannenbaum, *Carbon*, 2013, 52, 56-64.

32. O. Vargas, Á. Caballero and J. Morales, *Electrochim. Acta.*, 2014, 130, 551-558.

33. S. C. Warren, K. Voïtchovsky, H. Dotan, C. M. Leroy, M. Cornuz, F. Stellacci, C. Hébert, A. Rothschild and M. Grätzel, *Nat. Mater.*, 2013, 12, 842-849.

34. D. Ramimoghadam, S. Bagheri and S. B. A. Hamid, *J. Magn. Magn. Mater.*, 2014, 368, 207-229.

35. A. Recnik, I. Nyiro-Kosa, I. Dodony and M. Posfai, *CrystEngComm*, 2013, 15, 7539-7547.

36. K. K. A. W. Mader, *Z. Naturforsch. B.*, 2006, 61, 665-671.

37. N. S. Chaudhari, S. S. Warule, S. Muduli, B. B. Kale, S. Jouen, B. Lefez, B. Hannoyer and S. B. Ogale, *Dalton Trans.*, 2011, 40, 8003-8011.

38. X. Yang, C. Chen, J. Li, G. Zhao, X. Ren and X. Wang, *R. Soc.Chem. Adv.*, 2012, 2, 8821-8826.

39. C. J. Serna and M. P. Morales, *Surf. ColloidSci.*, eds. E. Matijević and M. Borkovec, Springer US, 2004, vol. 17, ch. 2, pp. 27-81.

40. G. Wang, Z. Gao, G. Wan, S. Lin, P. Yang and Y. Qin, *Nano Res.*, 2014, 7, 704-716.

41. S. Oh, D. C. Cook and H. E. Townsend, *Hyperfine Interact.*, 1998, 112, 59-66.

42. I. T. Lucas, E. Dubois, J. Chevalet and S. Durand-Vidal, *Phys.Chem. Chem. Phys.*, 2008, 10, 3263-3273.

43. A. M. Jubb and H. C. Allen, *ACS Appl. Mater. Interfaces.*, 2010, 2, 2804-2812.

44. H. Zhang, X. Lv, Y. Li, Y. Wang and J. Li, *ACS Nano*, 2009, 4, 380-386.

45. H. N. Tien, V. H. Luan, L. T. Hoa, N. T. Khoa, S. H. Hahn, J. S. Chung, E. W. Shin and S. H. Hur, *Chem. Eng. J.*, 2013, 229, 126-133.

46. S. Mao, Z. Wen, T. Huang, Y. Hou and J. Chen, *Energy. Environ. Sci.*, 2014, 7, 609-616.

47. F. Meng, J. Li, S. K. Cushing, J. Bright, M. Zhi, J. D. Rowley, Z. Hong, A. Manivannan, A. D. Bristow and N. Wu, *ACS Catal.*, 2013, 3, 746-751.

48. J. Zhou, H. Song, L. Ma and X. Chen, *R. Soc.Chem. Adv.*, 2011, 1, 782-791.

49. S. L. Tait, Y. Wang, G. Costantini, N. Lin, A. Baraldi, F. Esch, L. Petaccia, S. Lizzit and K. Kern, *J. Am. Chem. Soc.*, 2008, 130, 2108-2113.

50. G. Wang, Y. Ling, D. A. Wheeler, K. E. N. George, K. Horsley, C. Heske, J. Z. Zhang and Y. Li, *Nano Lett.*, 2011, 11, 3503-3509.

51. A. Mettenbörger, T. Singh, A. P. Singh, T. T. Järvi, M. Moseler, M. Valldor and S. Mathur, *Int. J. Hydrogen Energy.*, 2014, 39, 4828-4835.

52. Y.S. Hu, A. Kleiman-Shwarsctein, A. J. Forman, D. Hazen, J.-N. Park and E. W. McFarland, *Chem. Mater.*, 2008, 20, 3803-3805.

53. S. U. M. Khan and J. Akikusa, *J. Phys. Chem. B.*,1999, 103, 7184-7189.

54. S. Kumari, A. P. Singh, C. Tripathi, D. Chauhan, S. Dass, R. Shrivastav, V. Gupta, K. Sreenivas and V. R. Satsangi, *Int. J. Photoenergy.*, 2007, 2007, 1-6.

55. C.-Y. Chang, C.-H. Wang, C.-J. Tseng, K.-W. Cheng, L.-W. Hourng and B. T. Tsai, *J. Hydrogen Energy.*, 2012, 37, 13616-13622.

56. K. Zhang, X. Shi, J. K. Kim, J. S. Lee and J. H. Park, *Nanoscale*, 2013, 5, 1939-1944.

57. J. Young Kim, J.-W. Jang, D. Hyun Youn, J. Yul Kim, E. Sun Kim and J. Sung Lee, *R. Soc.Chem. Adv.*, 2012, 2, 9415-9422.

58. J. Y. Kim, G. Magesh, D. H. Youn, J.-W. Jang, J. Kubota, K. Domen and J. S. Lee, *Sci. Rep.*, 2013, 3, 1-8.

RSC Advances Accepted Manuscript